


## Article

# Highly Efficient NO<sub>2</sub> Sensors Based on Al-ZnOHF under UV Assistance

Xingyu Yao <sup>1</sup>, Rutao Wang <sup>1</sup>, Lili Wu <sup>1,\*</sup>, Haixiang Song <sup>2</sup>, Jinbo Zhao <sup>3</sup>, Fei Liu <sup>1</sup>, Kaili Fu <sup>1</sup>, Zhou Wang <sup>1</sup>, Fenglong Wang <sup>1</sup> and Jiurong Liu <sup>1</sup>

<sup>1</sup> Key Laboratory for Liquid-Solid Structural Evolution and Processing of Materials, Ministry of Education and School of Materials Science and Engineering, Shandong University, Jinan 250061, China; xinghuiyxy@gmail.com (X.Y.)

<sup>2</sup> Henan Joint International Research Laboratory of Nanocomposite Sensing Materials, School of Chemical and Environmental Engineering, Anyang Institute of Technology, Anyang 455000, China

<sup>3</sup> School of Materials Science and Engineering, Qilu University of Technology (Shandong Academy of Sciences), Jinan 250353, China

\* Correspondence: wulili@sdu.edu.cn

**Abstract:** Zinc hydroxyfluoride (ZnOHF) is a newly found resistive semiconductor used as a gas-sensing material with excellent selectivity to NO<sub>2</sub> because of its unique energy band structure. In this paper, Al<sup>3+</sup> doping and UV radiation were used to further improve the gas-sensing performance of ZnOHF. The optimized 0.5 at.% Al-ZnOHF sample exhibits improved sensitivity to 10 ppm NO<sub>2</sub> at a lower temperature (100 °C) under UV assistance, as well as a short response/recovery time (35 s/96 s). The gas-sensing mechanism demonstrates that Al<sup>3+</sup> doping increases electron concentration and promotes electron transfer of the nanorods by reducing the bandgap of ZnOHF, and the photogenerated electrons and holes with high activity under UV irradiation provide new reaction routes in the gas adsorption and desorption process, effectively promoting the gas-sensing process. The synergistic effect of Al<sup>3+</sup> and UV radiation contribute to the enhanced performance of Al-ZnOHF.

**Keywords:** gas sensors; Al<sup>3+</sup>-doped; ZnOHF; NO<sub>2</sub>; UV assistance



**Citation:** Yao, X.; Wang, R.; Wu, L.; Song, H.; Zhao, J.; Liu, F.; Fu, K.; Wang, Z.; Wang, F.; Liu, J. Highly Efficient NO<sub>2</sub> Sensors Based on Al-ZnOHF under UV Assistance. *Materials* **2023**, *16*, 3577. <https://doi.org/10.3390/ma16093577>

Academic Editor: Lado Filipovic

Received: 5 April 2023

Revised: 26 April 2023

Accepted: 4 May 2023

Published: 7 May 2023



**Copyright:** © 2023 by the authors. Licensee MDPI, Basel, Switzerland. This article is an open access article distributed under the terms and conditions of the Creative Commons Attribution (CC BY) license (<https://creativecommons.org/licenses/by/4.0/>).

## 1. Introduction

As a typical pollution gas, nitrogen dioxide (NO<sub>2</sub>) seriously threatens human health and the environment [1,2]. Exposure to NO<sub>2</sub> with a concentration of over 200 µg/m<sup>3</sup> in the short term or over 40 µg/m<sup>3</sup> in the long term will pose a serious threat to the normal operation of the respiratory system [3]. Additionally, NO<sub>2</sub> is also the main source of acid rain and photochemical smog. Hence, the development of gas sensors for efficiently detecting the concentration of NO<sub>2</sub> in the atmosphere is highly significant and essential. In the research on NO<sub>2</sub> sensors, resistance gas sensors stand out among different kinds of gas sensors due to their excellent sensitivity, selectivity, and stability [4–6], as well as their relatively low cost and easy operation [7]. As the core part of sensors, the sensing materials directly determine the performance of gas sensors.

Zinc hydroxyfluoride (ZnOHF) is a new type of semiconductor discovered in recent years which has gradually attracted the attention of researchers in various fields, such as photocatalysts [8,9], ultrasonic degradation [10] and solar cells [11], for its unique crystal and energy band structure [12,13]. In our previous research, we found that ZnOHF is an excellent gas-sensing material with good selectivity to NO<sub>2</sub> gas [14]. The unique energy band structure of ZnOHF inhibits the adsorption and dissociation of oxygen molecules on its surface, and the little absorbed oxygen species on the surface of ZnOHF lead to its wide detection range to NO<sub>2</sub>, which makes ZnOHF a good candidate for NO<sub>2</sub> detection among resistive semiconductors. However, the gas sensors based on ZnOHF still have room for

improvement in performance; for example, the operating temperature of ZnOHF-based gas sensors is still high, and its sensitivity still has a certain gap compared with many other NO<sub>2</sub>-sensing materials. Therefore, further improvement for ZnOHF to obtain better sensing performance is necessary.

Light-activated gas sensors have been widely studied as an effective improvement method in recent years. Under the assistance of light irradiation, there will be more electrons and holes with high activity generated on the surface of materials, which is beneficial to the adsorption and desorption of target gases [15,16]. Wang et al. [17] found that ZnO nanoplates exhibited a great enhancement in sensitivity and recovery time in NO<sub>2</sub> detection under intermittent UV irradiation. This phenomenon can be explained by the competitive adsorption of NO<sub>2</sub> and O<sub>2</sub> and the modulating action of gas adsorption. Zhang and his group [18] grew TiO<sub>2</sub> nanoplates in situ with a highly active crystal plane on MXene (Ti<sub>3</sub>C<sub>2</sub>T<sub>x</sub>) and obtained greatly enhanced gas-sensing performance to NH<sub>3</sub> under UV light. The density functional theory revealed that this composite structure exhibits the highest adsorption affinity to NH<sub>3</sub> with UV light assistance. Additionally, Tai's group [19] also applied gamma-ray in NO<sub>2</sub> detection, and they found that it can effectively enhance the sensitivity of ZnO nanorods at room temperature by constructing lots of defects. Bang et al. [20] presented a proton-beam irradiation method to engineer surface-point defects on ZnO in order to improve the preferential adsorption on the surface compared to water molecules so that it can detect NO<sub>2</sub> with less humidity interference. As a kind of photocatalyst, ZnOHF has excellent photochemical properties, including suitable band gaps and strong light absorbance, which makes it possible to act as a better gas sensor of NO<sub>2</sub> under UV radiation [21,22].

Ion doping is a promising approach in gas-sensing performance improvement. On the one hand, doping ions with different quantities of charges can effectively adjust the carrier concentration and energy band structure of semiconductors [23,24]. On the other hand, due to the difference in diameters between doping ions and original ions, ion doping can create lots of lattice imperfections. Some imperfections can act as efficient adsorption sites of oxygen molecules or target gas molecules, thus improving their gas-sensing performance [25]. Qin and his colleague [26] synthesized metal-organic-frameworks-derived Mn-doped Co<sub>3</sub>O<sub>4</sub> porous nanosheets, which exhibited better CO-sensing performance than pure Co<sub>3</sub>O<sub>4</sub> because of the oxygen vacancies generated in the ion doping process. Mokrushin et al. [27] doped Eu and Pr ions into ZnO powders and found that it not only improved the sensitivity but also obtained great humidity resistance performance. Cr<sup>3+</sup>-doped In<sub>2</sub>O<sub>3</sub> was prepared by Sun et al. [28], and this material shows high sensitivity, a low detection limit, and short response/recovery time in NH<sub>3</sub> sensing due to the increase in active sites and reduced material resistance. Al<sup>3+</sup> ion is one of the common doping ions utilized in zinc-based materials' modification. Since Al<sup>3+</sup> has a higher charge than Zn<sup>2+</sup>, Al<sup>3+</sup> doping can increase electron concentration, which will benefit the gas-sensing process [29,30]. Moreover, Al<sup>3+</sup> has a similar diameter to Zn<sup>2+</sup>, indicating that Al<sup>3+</sup> doping will not seriously damage the crystal structure of the host ZnOHF [31,32].

Herein, Al-ZnOHF nanorods with optimized Al<sup>3+</sup> concentrations were prepared through a simple hydrothermal method. The NO<sub>2</sub>-sensing performance of Al<sup>3+</sup>-doped samples is significantly improved compared with pure ZnOHF under UV irradiation with a wavelength of 395 nm and a strength of 6 mW/cm<sup>2</sup>. Additionally, especially, the 0.5 at.% Al-ZnOHF sample exhibits the best gas-sensing properties. The NO<sub>2</sub>-sensing mechanism analysis revealed that the bandgap narrowing and improvement in UV absorbance after Al<sup>3+</sup> doping are the main reasons for its performance enhancement.

## 2. Materials and Methods

### 2.1. Chemicals

All chemicals utilized in this work, including zinc acetate (Zn(CH<sub>3</sub>COO)<sub>2</sub>•2H<sub>2</sub>O), ammonium fluoride (NH<sub>4</sub>F), aluminum nitrate (Al(NO<sub>3</sub>)<sub>3</sub>•9H<sub>2</sub>O), and hexamethylenete-

tramine (HMT), were purchased from Sinopharm Chemical Reagent Co., Ltd. (Shanghai, China) and were of analytical grade, which can be used without any purification.

## 2.2. Synthesis of Al<sup>3+</sup>-doped ZnOHF

Al-ZnOHF nanorods with different molar ratios of Al<sup>3+</sup> (0 at.%, 0.1 at.%, 0.2 at.%, 0.5 at.%, and 1 at.%) were synthesized via a simple hydrothermal method. Initially, 0.65 g Zn(CH<sub>3</sub>COO)<sub>2</sub>•2H<sub>2</sub>O, 0.42 g HMT and 0.051 g NH<sub>4</sub>F were dissolved in 15 mL of distilled water successively with continuous stirring to form a homogeneous solution. Different amounts of Al(NO<sub>3</sub>)<sub>3</sub>•9H<sub>2</sub>O were then added to the mixture with continuous stirring. After stirring for another 0.5 h, the solution was transferred into 20 mL Teflon-lined autoclaves and heated at 368 K for 2 h. The products were collected, purged with distilled water and ethyl alcohol, and then dried at 340 K for 6 h.

## 2.3. Characterizations

The crystal structures of samples were tested through X-ray powder deflection (XRD, DMAX-2500PC, Regaku, Japan) equipped with Cu-K $\alpha$  ( $\lambda = 1.542 \text{ \AA}$ ) radiation with a step size of  $0.02^\circ$  and a scan rate of  $10^\circ/\text{min}$  in the range of  $10\text{--}90^\circ$ . The surface morphologies and micro-structure characterizations were carried out by scanning electron microscopy (SEM, SU-70, Hitachi, Japan) operated at an accelerating voltage of 15 kV and transmission electron microscopy (TEM, JEM 2100, JEOL Ltd., Akishima, Japan) operated at 200 kV. X-ray photoelectron spectrometer (XPS, AXIS Supra, Kratos, Japan) measurement (equipped with monochromatic Al-K $\alpha$  radiation,  $h\nu = 1486.6 \text{ eV}$ ) was utilized to analyze the valence state of elements and the chemical environment of atoms on the surface of samples. The UV-vis diffuse reflection spectrum (UV-vis DRS) was recorded on Agilent Cary 300/PE lambda 750S (America) ultraviolet spectrophotometer and was used to test UV absorption and bandgap of the samples.

## 2.4. Gas-Sensing Properties Test

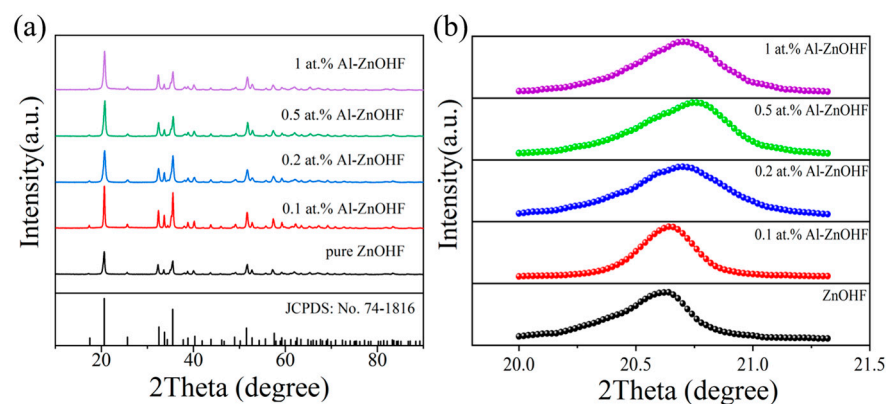
The preparation method of gas-sensing units was explained as follows. First, the as-prepared samples were dispersed into distilled water with a weight ratio of 1:5 and treated with ultrasound for 10 min. Additionally, the slurry was dropped on the Al<sub>2</sub>O<sub>3</sub> substrate, which has four Pt wires as the electrodes, and was dried at  $80^\circ\text{C}$ . After repeating this step 2–4 times, the substrate was annealed at  $200^\circ\text{C}$  for 3 h and then the electrodes were welded on the pedestal to form a gas-sensing unit. After that, the sensor was aged at 4 V for 7 days before the gas-sensing test. The gas-sensing properties of gas sensors based on various samples were tested via a WS-30B gas sensitivity instrument (Zhengzhou Winsen Electronics Co., Ltd., Zhengzhou, China) at an environmental temperature of  $25^\circ\text{C}$  and humidity of 20–30%. The UV light was provided by LED light with wavelength of 395 nm (Ceaulight Co., Beijing, China). The response value of sensors (S) is calculated as  $S = R_g/R_a$  for oxidizing gases and  $S = R_a/R_g$  for reducing gases, where  $R_a$  and  $R_g$  are the resistance of the sensor in air and target gases, respectively. Additionally, the response and recovery times are defined as the times from gas input or pumped out until the response value changes to 90% of its maximum value.

# 3. Results and Discussion

## 3.1. Characterization

Figure 1 shows the XRD patterns of Al-ZnOHF with different amounts of aluminum ions. The diffraction peaks of each sample could be approximately matched with the standard data of orthorhombic-phase ZnOHF (JCPDS No: 74-1816). After the addition of Al<sup>3+</sup>, the central position of diffraction peaks changed significantly. It can be seen in the magnified region around the strongest peak (Figure 1b) that the peak trended to a higher angle with the increase in Al<sup>3+</sup> concentration at first, indicating that the Al<sup>3+</sup> with the size of 0.0535 nm may occupy some positions of the Zn<sup>2+</sup> with the size of 0.074 nm. Additionally, then, the peak turned back to the lower angle (1 at.% Al-ZnOHF), indicating that the Al<sup>3+</sup>

dopes into the interstitial void of the ZnOHF lattice, which results in the broadening of the interplanar crystal spacing.



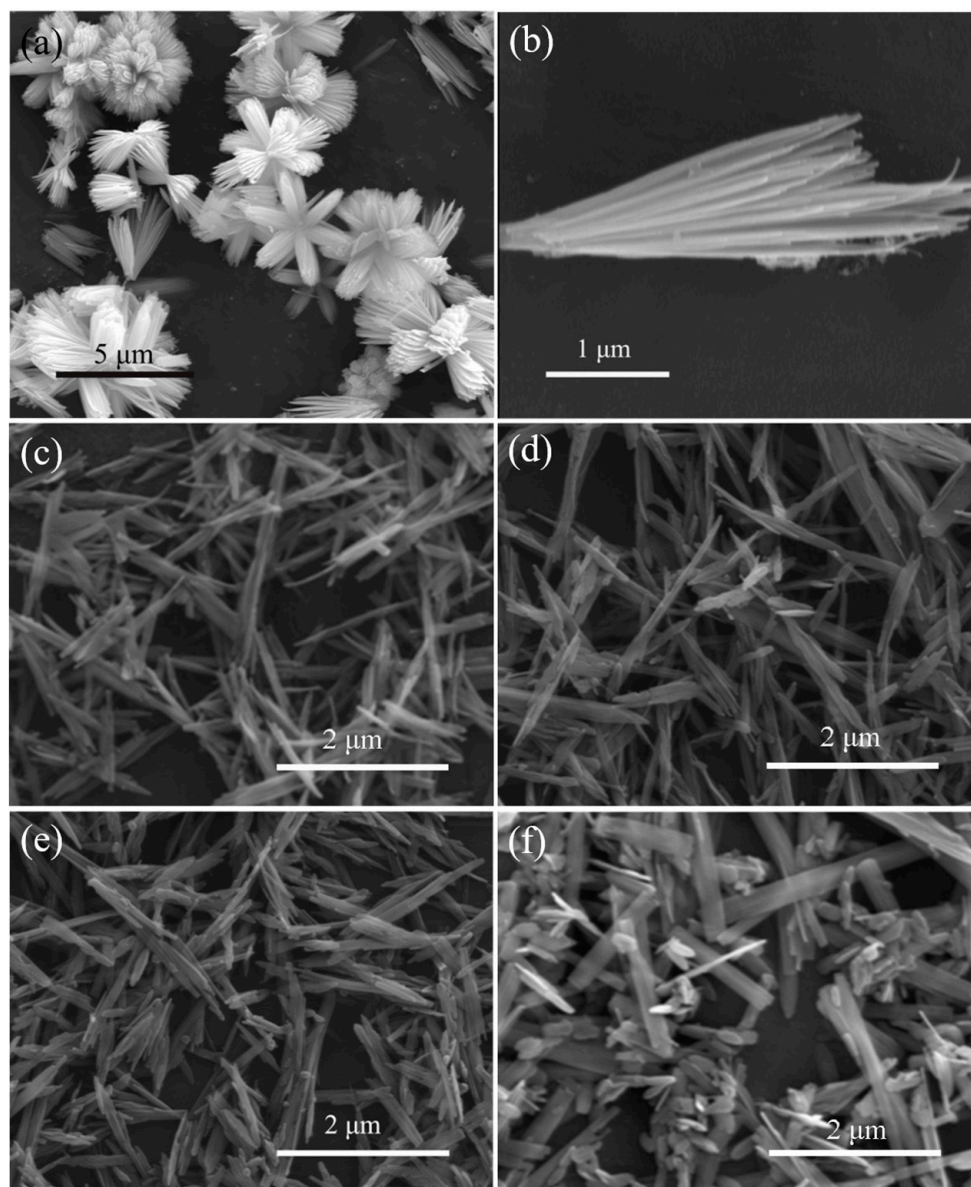
**Figure 1.** (a) The XRD spectra and (b) magnified region of the strongest peak of all Al-ZnOHF samples.

Figure 2a,b shows the SEM images of pure ZnOHF. The basic structure of pure ZnOHF is nanorods, and the ends of these nanorods are gathered together to constitute flower-like structures with sizes ranging from 3 to 5  $\mu\text{m}$ . SEM graphs of samples with different  $\text{Al}^{3+}$  dopings are exhibited in Figure 2c–f. After  $\text{Al}^{3+}$  doping, the flower-like structures of pure ZnOHF change into irregular bundles, which also consist of nanorods. With the increase in the amount of  $\text{Al}^{3+}$ , the length of bundles gradually shortened and thickened, and the morphology gradually changed to microbelts. Additionally, lots of small nanoplates also appeared, and the quantity gradually increased with the increase in  $\text{Al}^{3+}$  content. Finally, when the  $\text{Al}^{3+}$  doping amount reached 1 at.%, the morphology of the sample was mainly composed of long microbelts and plenty of nanoplates.

To further analyze the microstructure of the obtained samples, TEM and HRTEM images of pure ZnOHF and 0.5 at.% Al-ZnOHF are shown in Figure 3. As shown in Figure 3a,b, pure ZnOHF exhibits a regular nanorods-assembled flower-like structure. The HRTEM image (Figure 3c) shows that the diameter of nanorods is about 14 nm. Additionally, the lattice fringe spacing of pure ZnOHF could be measured as 0.25 nm, corresponding to the (1 1 1) crystal plane of ZnOHF. After  $\text{Al}^{3+}$  doping, the morphology of samples changed greatly (Figure 3d,e), which is in accord with the SEM images. Instead of forming a flower-like structure, the nanorods were clustered into bundles and scattered irregularly. The HRTEM image of 0.5 at.% Al-ZnOHF (Figure 3f) exhibits that the diameter of nanorods slightly increased to 25 nm. Its lattice fringe spacing was calculated to be 0.42 nm, a little smaller than that of the (1 1 0) crystal plane. Hence,  $\text{Al}^{3+}$  doping changed the exposed surface crystal plane of samples and reduced the crystalline interplanar spacing.

The surface chemical properties of 0.5 at.% Al-ZnOHF were determined via X-ray photoelectron spectroscopy (XPS). As shown in Figure 4a, all 3 main elements (Zn, O, F) can be easily found in the wide XPS spectrum of both pure ZnOHF and 0.5 at.% Al-ZnOHF, and there is also a tiny peak at about 75 eV in the spectra of 0.5 at.% Al-ZnOHF, which can be matched with the Al element. The Zn 2p spectrum in Figure 4b shows that there are 2 peaks centered at 1021.8 eV and 1044.8 eV, corresponding to the  $\text{Zn}^{2+}$  orbits, 2p<sub>3/2</sub> and 2p<sub>1/2</sub>, respectively [33]. The peaks of F 2p (Figure 4c) of these 2 samples are centered at about 684.8 eV, matching well with  $\text{F}^-$  in the crystal lattice [34]. By comparison, the peaks of Zn and F of these two samples are approximately the same, meaning that  $\text{Al}^{3+}$  doping does not change the chemical environment of Zn and F atoms. The difference between these two samples at the high-resolution XPS regions of Al 2p and O 1s is shown in Figure 4d–e. The 0.5 at.% Al-ZnOHF exhibits a significant peak at about 75.2 eV, which can be indexed with  $\text{Al}^{3+}$  [35], while pure ZnOHF just shows a gentle background curve in this region (Figure 4d). This difference confirmed that Al ions were successfully doped into ZnOHF.

The O 1s peaks of both pure ZnOHF and 0.5 at.% Al-ZnOHF can be deconvoluted into two Gaussian peaks, which are matched with lattice oxygen and adsorbed oxygen species, respectively (Figure 4e) [14,36]. It is significant that the proportion of adsorbed oxygen species of 0.5 at.% Al-ZnOHF is higher than that of pure ZnOHF, confirming that Al<sup>3+</sup> doping promotes the surface adsorption of oxygen. In addition, the peaks of the 2 oxygen species exhibit a slight blueshift after Al<sup>3+</sup> doping (O<sub>latt.</sub> move from 532.0 eV to 531.6 eV and O<sub>ads.</sub> move from 532.8 eV to 532.2 eV). This phenomenon may be ascribed to the weaker adsorption capacity for electrons of Al<sup>3+</sup> than that of Zn<sup>2+</sup>. When Al<sup>3+</sup> substitutes the Zn<sup>2+</sup> in the lattice, the electron density increases due to the construction of the Al-O bond [37–39]. Therefore, Al<sup>3+</sup> doping can decrease the binding energy of electrons of oxygen species and obtain adsorbed oxygen with higher activity.



**Figure 2.** SEM images of (a,b) pure ZnOHF, (c) 0.1 at.% Al-ZnOHF, (d) 0.2 at.% Al-ZnOHF, (e) 0.5 at.% Al-ZnOHF, (f) 1 at.% Al-ZnOHF.

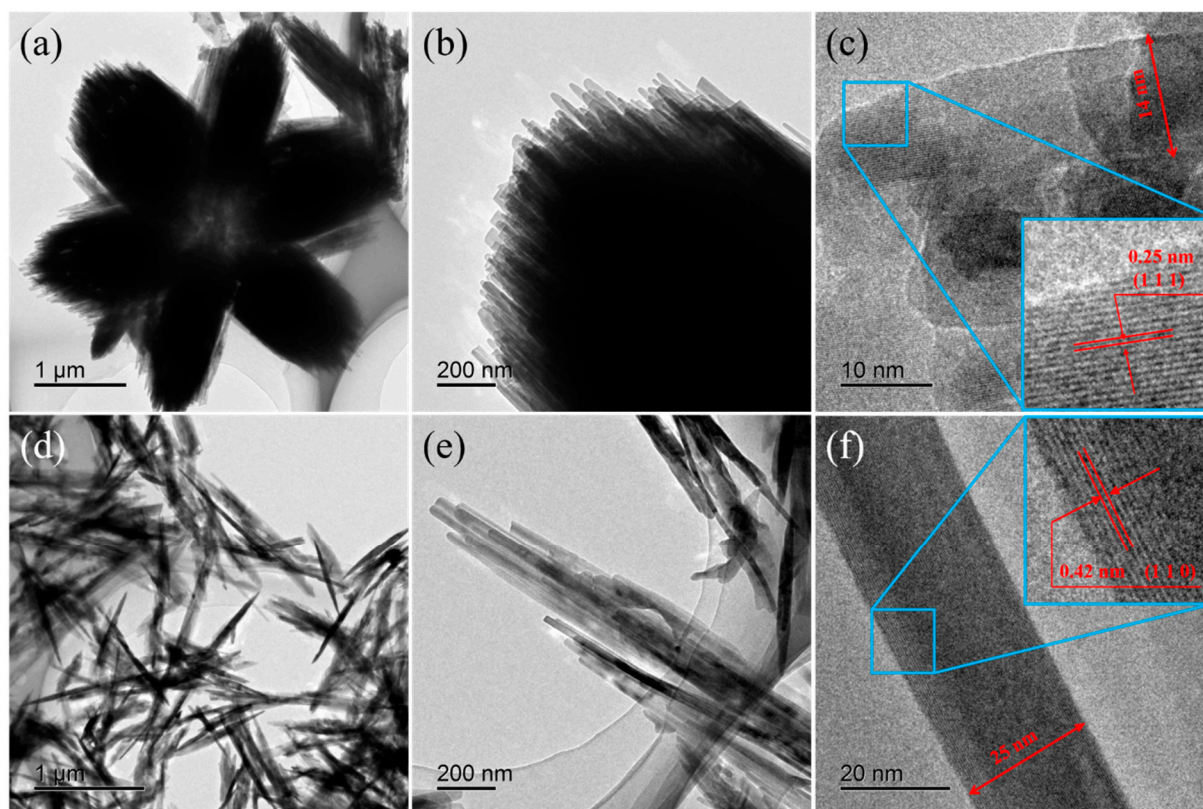


Figure 3. TEM and HRTEM images of (a–c) pure ZnOHF, (d–f) 0.5 at.% Al-ZnOHF.

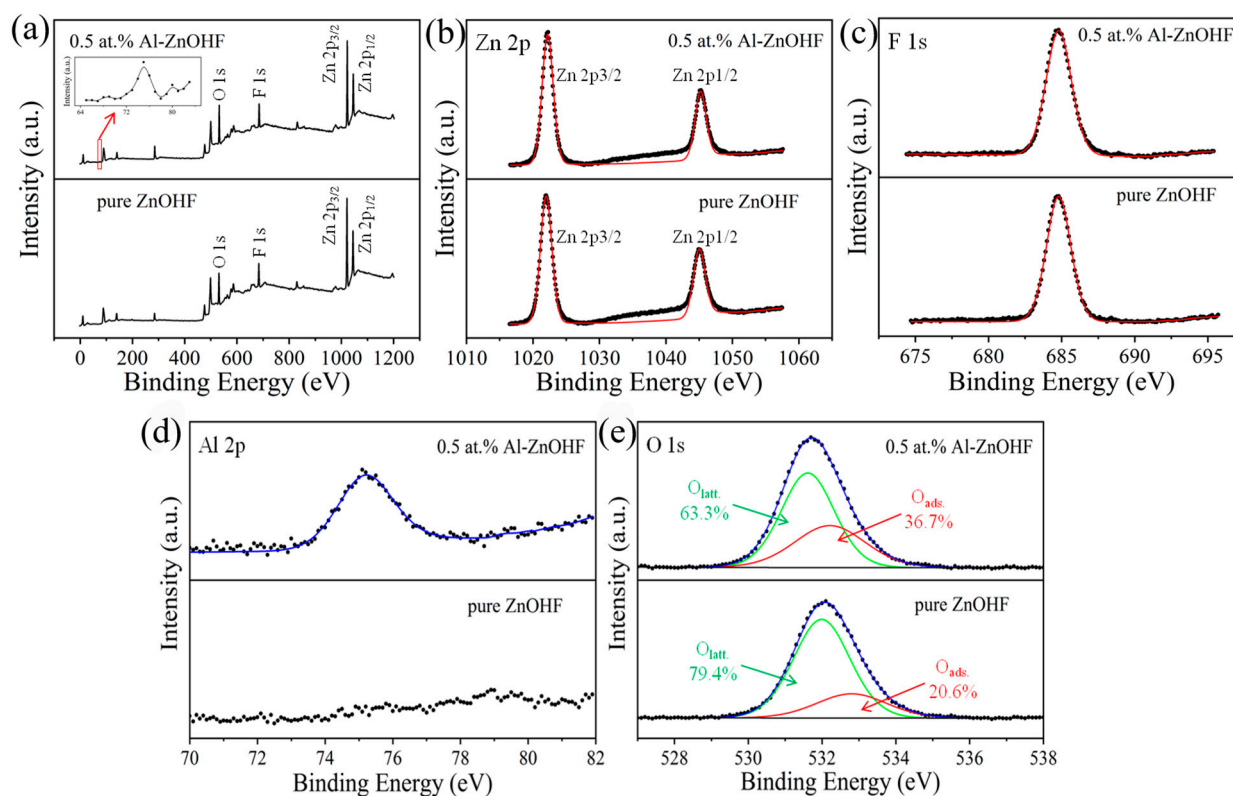
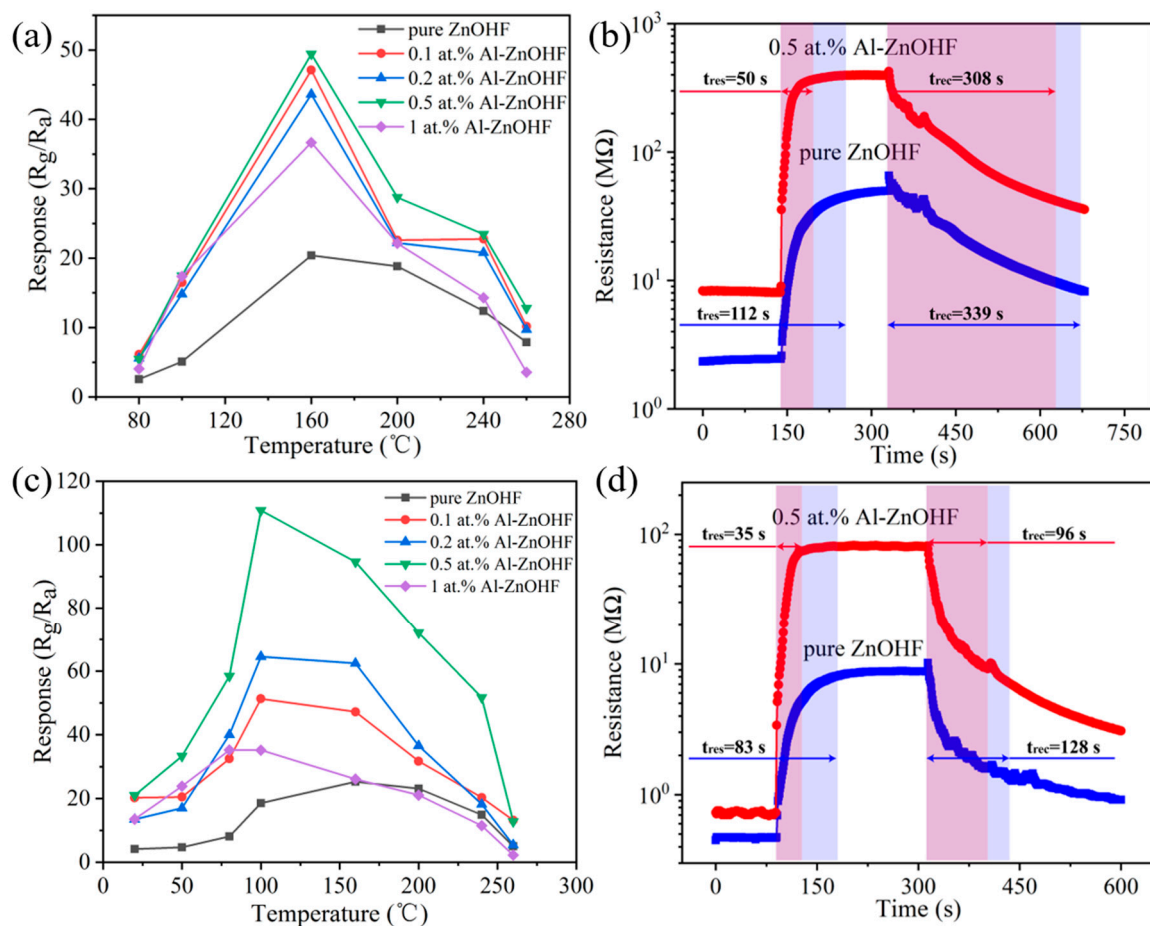


Figure 4. (a) XPS wide spectrum, (b) Zn 2p region, (c) F 1s region, (d) Al 2p region, and (e) O 1s region XPS spectra of pure ZnOHF and 0.5 at.% Al-ZnOHF. (the dots are test data and the red and blue lines are fixed curves).

### 3.2. Gas-Sensing Properties

The gas-sensing properties of ZnOHF with various amounts of Al<sup>3+</sup> doping were tested under different temperatures (Figure 5a). Due to the low thermal stability of ZnOHF at high temperatures (it decomposes into ZnO and HF at over 300 °C) [14], the test temperature should be controlled under 300 °C. Significantly, the best operating temperatures of all samples are 160 °C. The response value of Al<sup>3+</sup>-doped samples shows various levels of increase compared with pure ZnOHF. Especially, gas sensors based on 0.5 at.% Al-ZnOHF obtained the highest response (49.43) to 10 ppm NO<sub>2</sub>, 2.42 times higher than that of pure ZnOHF. In addition, the dynamic response curves of sensors based on 0.5 at.% Al-ZnOHF and pure ZnOHF to 10 ppm NO<sub>2</sub> are shown in Figure 5b. It is worth noting that the response time of 0.5 at.% Al-ZnOHF (50 s) is a little shorter than that of pure ZnOHF (112 s), but both of them exhibit extremely long recovery times or even cannot recover back to the previous resistance. The resistance of samples at different temperatures is shown in Figure S1a. It is evident that with the increase in the Al<sup>3+</sup> doping amount, the resistance of samples rises at first, probably due to the destruction of the regular morphology of pure ZnOHF after ion doping, which is not conducive to electron conduction. Additionally, the resistance reduces when the Al<sup>3+</sup> doping amount continuously increases because of the increase in carrier concentration. The extremely high resistance of samples also seriously restricts the gas-sensing test at low temperatures.



**Figure 5.** (a) Gas responses of all obtained samples to 10 ppm NO<sub>2</sub> at different temperatures in the dark. (b) The response–recovery curves of pure ZnOHF and 0.5 at.% Al-ZnOHF to 10 ppm NO<sub>2</sub> at 160 °C in dark. (c) Gas responses of all obtained samples to 10 ppm NO<sub>2</sub> at different temperatures under UV assistance. (d) The response–recovery curves of pure ZnOHF and 0.5 at.% Al-ZnOHF to 10 ppm NO<sub>2</sub> at 100 °C under UV assistance.

To solve this problem, UV-light radiation was utilized in the gas-sensing process. It can be seen in Figure S1b that the resistance of all samples significantly decreases under UV radiation, and the Al<sup>3+</sup>-doped samples obtained a higher reduction rate with higher UV absorbance. The gas-sensing properties of samples under UV light with the wavelength of 395 nm and strength of 6 mW/cm<sup>2</sup> at different temperatures were tested, as illustrated in Figure 5c. It is significant that the best operating temperature of 0.1, 0.2, and 0.5 at.% Al-ZnOHF is 100 °C, while that of 1 at.% Al-ZnOHF is 80 °C, indicating that the operating temperature decreased after UV radiation. Specifically, the sensor based on 0.5 at.% Al-ZnOHF exhibited the highest response, with a value of 110.83 to 10 ppm NO<sub>2</sub>, which is approximately 4 times higher than that of pure ZnOHF (25.29). Additionally, the best response values of 0.1 at.%, 0.2 at.%, and 1 at.% Al-ZnOHF are 51.32, 64.55, and 35.22, respectively. Therefore, as the concentration of Al<sup>3+</sup> goes up, the best operating temperature of samples exhibits a downtrend, and the sensitivity of ZnOHF increases initially and then decreases. Compared with the test results without UV light, the response of 0.5 at.% Al-ZnOHF to 10 ppm NO<sub>2</sub> under UV light exhibit over 2-fold promotion, while the responses of other samples only increased a little. As shown in Figure 5d, the response/recovery times of pure ZnOHF and 0.5 at.% Al-ZnOHF were 83 s/128 s and 35 s/96 s, respectively. Both of them were significantly reduced compared with that in the dark environment. Therefore, the 0.5 at.% Al-ZnOHF sample obtains a high response and fast response/recovery speed at 100 °C with UV assistance.

The dynamic sensing curve of 0.5 at.% Al-ZnOHF to NO<sub>2</sub> with various concentrations is shown in Figure 6a. With the increase in the gas concentration, the response value continuously rises, and the response/recovery time exhibits no apparent change. It is worth noting that the detection limit of 0.5 at.% Al-ZnOHF is 0.25 ppm, with a response value of 2.18, which is higher than that of pure ZnOHF, as shown in Figure S2a (1.57 to 0.25 ppm NO<sub>2</sub>). Additionally, the dynamic response curve of these two samples in the dark (Figure S2b,c) exhibits that the detection limits of pure ZnOHF and 0.5 at.% Al-ZnOHF in dark are 0.5 ppm. Therefore, UV light effectively reduces the detection limit of Al-ZnOHF samples. The relationship between NO<sub>2</sub> concentration and the response value of pure ZnOHF and 0.5 at.% Al-ZnOHF is shown in Figure 6b, respectively. Significantly, the logarithm of gas concentration and response value of both samples shows an excellent linear relationship with high reliability. Additionally, the slope of the fitted curve of 0.5 at.% Al-ZnOHF is higher than that of pure ZnOHF. This phenomenon means that when exposing a sensor based on 0.5 at.% Al-ZnOHF to NO<sub>2</sub>; a slight change in gas concentration will lead to a more dramatic change of response value than that of pure ZnOHF, which can be explained by the following equation.

$$\frac{d[S]}{d[C]} = \frac{S}{C} \frac{d \ln[S]}{d \ln[C]}$$

Therefore, the gas sensor based on 0.5 at.% Al-ZnOHF can detect NO<sub>2</sub> more sensitively and accurately than pure ZnOHF.

Repeatability is also an essential feature of gas sensors. The dynamic sensing curve of 0.5 at.% Al-ZnOHF in 4 cycles was tested. As shown in Figure 6c, the response value and response/recovery time show no discernible difference in these cycles. Therefore, the 0.5 at.% Al-ZnOHF sensor exhibits superior repeatability to NO<sub>2</sub> gas at 100 °C under UV assistance. Moreover, the response values of 0.5 at.% Al-ZnOHF within one month remained relatively stable, as shown in Figure 6d, proving its great stability. In order to understand the interference of other gases in practical application, the gas-sensing test of the samples to other gases is shown in Figure 6e. Sensors based on both pure ZnOHF and 0.5 at.% Al-ZnOHF exhibit a high response to NO<sub>2</sub>, while the response values to other gases are lower than 2, indicating that both samples show excellent selectivity. Compared with many other zinc-based gas-sensing materials shown in Table 1, the Al-ZnOHF sample exhibits a great gas-sensing performance (high sensitivity, short response/recovery time, and low detection limit) at relatively low temperatures.



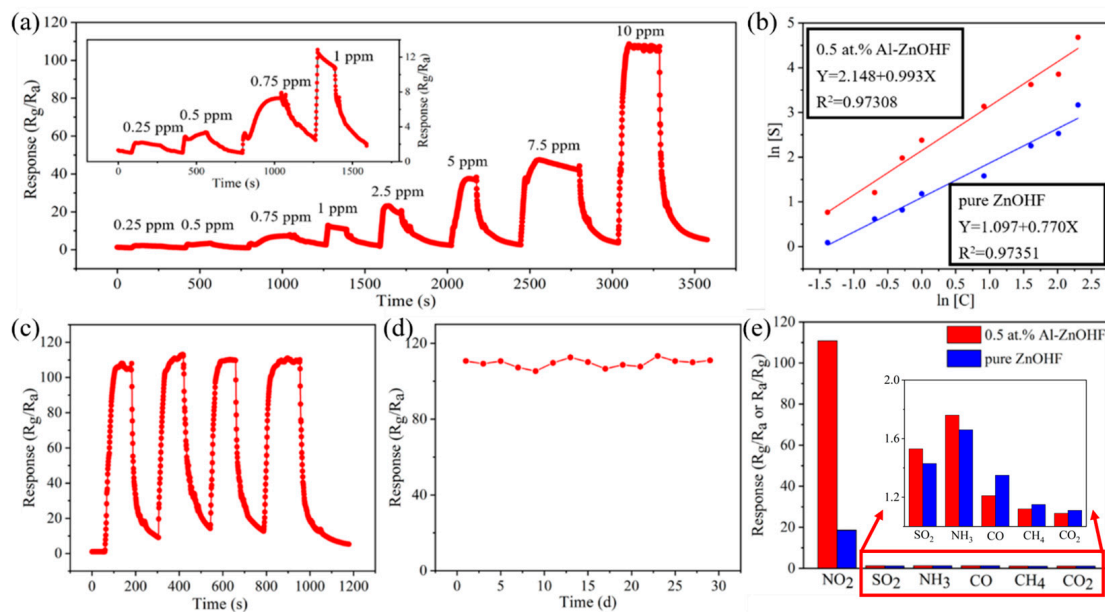


**Figure 6.** Under UV assistance and 100 °C: (a) the dynamic response curve of 0.5 at.% Al-ZnOHF; (b) the linear relationship between the logarithm of response value and the logarithm of gas concentration of pure ZnOHF (blue) and Al-ZnOHF (red); (c) response–recovery curve in 4 cycles of 0.5 at.% ZnOHF; (d) the response change of 0.5 at.% ZnOHF at 1 month, and (e) response value of pure ZnOHF and 0.5 at.% Al-ZnOHF to 10 ppm NO<sub>2</sub>, SO<sub>2</sub>, NH<sub>3</sub>, CO, CH<sub>4</sub> and CO<sub>2</sub>.

**Table 1.** The NO<sub>2</sub>-sensing performance of materials in references and this work.

Materials	Operating Condition	S (R <sub>g</sub> /R <sub>a</sub> or R <sub>a</sub> /R <sub>g</sub> )	T <sub>res</sub> /T <sub>rec</sub> (s)	Detection Limit	Ref.
ZnO/SnO <sub>2</sub> composite	40 °C, UV (395 nm, 34 μW/cm <sup>2</sup> )	25 (1 ppm)	251/470	100 ppb	[40]
Ag-ZnO nanoparticles	25 °C, visible light (455 nm, 70 mW/cm <sup>2</sup> )	2.5 (5 ppm)	200/175	1 ppm	[41]
Si-ZnO thin films	75 °C, purple-blue (430 nm)	19.1 (400 ppb)	60/180	-	[42]
CeO <sub>2</sub> /ZnO nanorods	120 °C	190.6% (5 ppm)	104/417	100 ppb	[43]
Fe <sub>2</sub> O <sub>3</sub> -ZnO nanostructures	300 °C	6.34 (10 ppm)	26/185	1 ppm	[44]
3D flower-like ZnOHF	200 °C	82.71 (10 ppm)	13/35	0.1 ppm	[14]
0.5 at.%Al-ZnOHF	100 °C, UV (395 nm, 6 mW/cm <sup>2</sup> )	110.83 (10 ppm)	35/96	0.25 ppm	This work

In practical application, the relative humidity of the gas testing environment is an important factor that affects gas-sensing properties at low operating temperatures. Relative humidity is defined as the ratio of the absolute humidity in the air to the saturated vapor pressure of water under the same condition. Figure 7a shows the sensing curves of the 0.5 at.% Al-ZnOHF sample at various relative humidities at 100 °C. Before the relative humidity reaches 50%, the response value of 0.5 at.% Al-ZnOHF remains relatively stable. When the relative humidity continues to rise, the response value shows a somewhat decline (Figure 7b). However, the response value of the sensor at RH95 was 73.79, still keeping about 67.0% of that at RH20. Figure 7c illustrates that the higher the relative humidity of the test environment is, the faster the response value's decline. In terms of the response time, with the relative humidity increasing, it rises a little while the recovery time increases to about 250 s (Figure 7c). Thinking of the low operating temperature of 100 °C, Al-ZnOHF exhibits a relatively great water-resistance performance, especially under relative humidity lower than RH50.

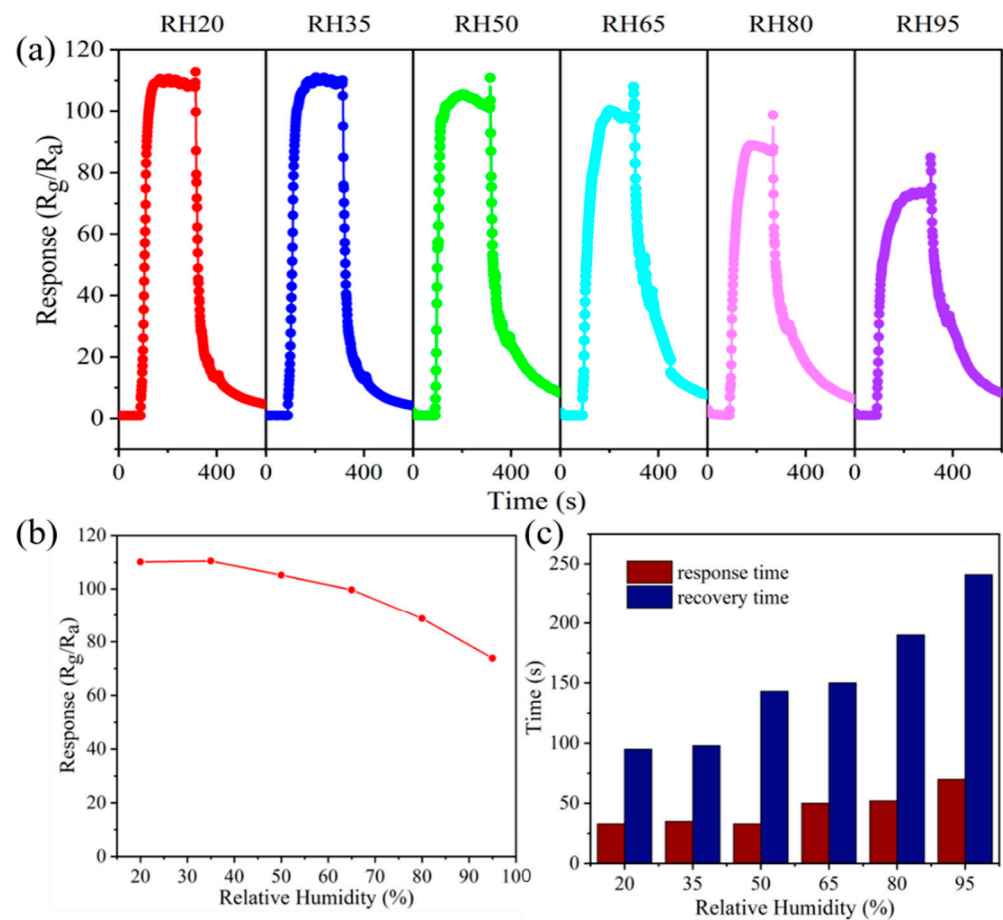


**Figure 7.** (a) The response–recovery curves, (b) the response value change, (c) response/recovery time of 0.5 at.% Al-ZnOHF to 10 ppm NO<sub>2</sub> at various relative humidities at 100 °C under UV radiation.

### 3.3. Gas-Sensing Mechanism

As an n-type semiconductor, the resistance of ZnOHF is mainly controlled by electrons in the conductive band. According to reference research, the resistance of gas-sensing material is mainly determined by the electron depletion layer on the surface, including its resistance and width [45,46]. Under relatively low temperatures, when exposing sensing material to air without photoactivation, some oxygen molecules adsorb on the surface and consume electrons to form oxygen ions ( $O_{2(ads)}^-$ , 0–150 °C), as shown in Reaction (1), thereby forming an electron depletion layer with high resistance [47]. When UV light is applied, for one thing, the surface adsorbed oxygen ions react with the photogeneration holes to release oxygen (Reaction (2)). For another, the physically adsorbed oxygen molecules capture photogeneration electrons to form new oxygen species with high activity (Reaction (3)). When these two reactions reach a balance, the surface of the material is coated with photoactivated oxygen ions [48].



The NO<sub>2</sub>-sensing process is shown in Figure 8. When exposing Al-ZnOHF sensors to NO<sub>2</sub> without UV light, the NO<sub>2</sub> molecules are ionized into NO<sub>2</sub><sup>-</sup> by capturing conductive band electrons, leading to an increase in resistance (Reaction (4)) [49]. In comparison, the UV-activated electrons are more active than those in the dark, making them easier

to combine with  $\text{NO}_2$  molecules (Reaction (5)). In addition, another reaction route will occur under UV light, as shown in Reaction (6). Some  $\text{NO}_2$  molecules also react with photoactivated oxygen ions and conductive band electrons to create  $\text{NO}_3^-$  [50]. Therefore, more  $\text{NO}_2$  will be adsorbed and reacted on the surface of Al-ZnOHF, and the sensitivity of the sensors demonstrates enormous improvement.

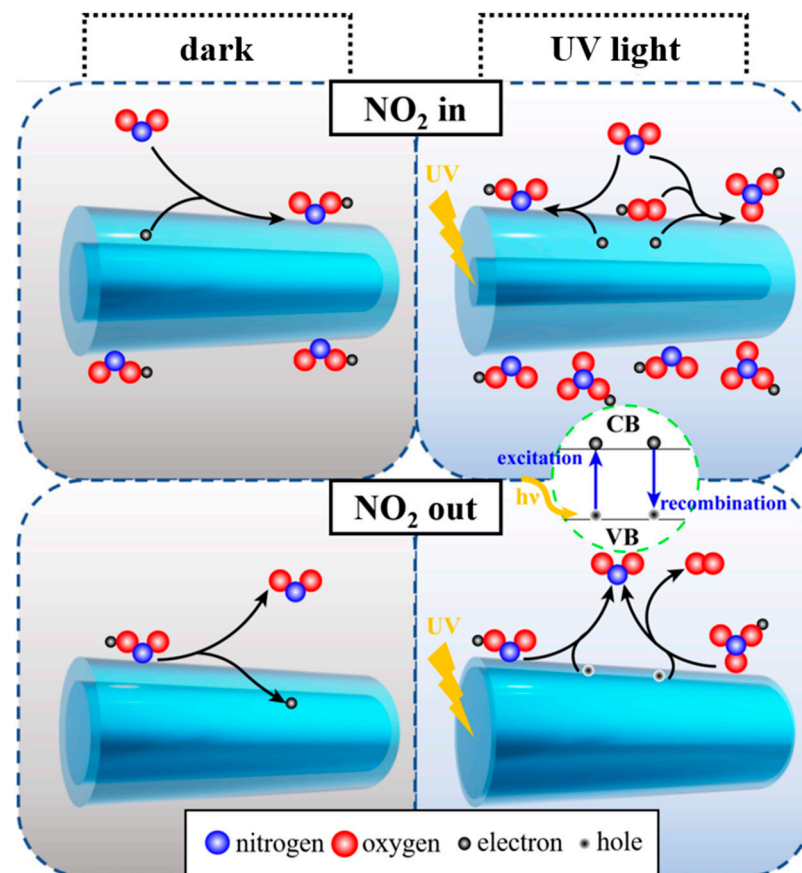
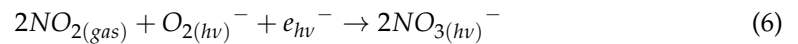
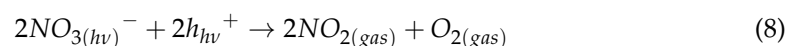
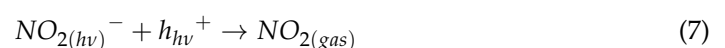


**Figure 8.** The response and recovery process of Al-ZnOHF in dark and with UV assistance.

When  $\text{NO}_2$  is pumped out, the surface-adsorbed ions are desorbed and release electrons to the conductive band of materials. The difference is that materials under UV light have a lot of photogenerated holes with high activity, which can efficiently promote the oxidation of  $\text{NO}_2^-$  and  $\text{NO}_3^-$  (Reactions (7) and (8)), as well as their desorption. Hence, UV light assistance can effectively accelerate the recovery process and reduce the recovery time [51,52].



In order to figure out the bandgap and UV light absorption of different samples, the UV-visible diffuse reflectance spectra of Al-ZnOHF with various  $\text{Al}^{3+}$  concentrations were tested (Figure 9a). Significantly, Al-ZnOHF exhibits a higher absorbance than pure ZnOHF, especially 0.5 at.% Al-ZnOHF. Using the T-plots of  $(\alpha h\nu)^2$  vs.  $h\nu$  of samples (Figure 9b),

the band gaps can be calculated as 3.31 eV for pure ZnOHF, 3.29 eV for 0.1 at.% Al-ZnOHF, 3.25 eV for 0.2 at.% Al-ZnOHF, 3.20 eV for 0.5 at.% Al-ZnOHF, and 3.40 eV for 1 at.% Al-ZnOHF. Hence, the introduction of a low content of Al<sup>3+</sup> can significantly narrow the bandgap of ZnOHF, and the 0.5 at.% Al-ZnOHF sample has the minimum bandgap. The UV absorption and bandgap are the main influencing factors of the generation of photoactivated electrons and holes, thereby affecting the gas-sensing process [37,53]. Therefore, compared with other samples, 0.5 at.% Al-ZnOHF exhibits the highest increase in the response value rate before and after UV light radiation.

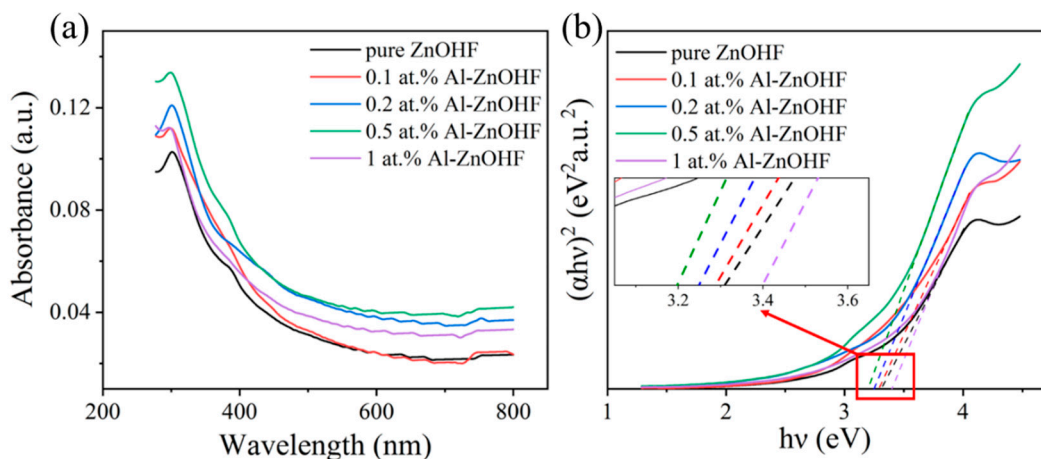


**Figure 9.** (a) The UV-vis diffuse reflectance spectra and (b) T-plots of  $(\alpha h\nu)^2$  vs.  $h\nu$  of all as-prepared samples (the dashed line is the tangent line of curves).

#### 4. Conclusions

In this work, Al-ZnOHF nanorods were synthesized via a simple one-step hydrothermal method for highly efficient NO<sub>2</sub>-sensing detection. Under UV light assistance, the gas sensitivity of 0.5 at.% Al-ZnOHF was further enhanced, and the response/recovery time was also significantly shortened. The sample preserved good anti-humidity performance, especially under RH50. The improvement in the gas-sensing performance of Al-ZnOHF can be ascribed to the reduced bandgap and increased electron concentration. UV irradiation generated electrons and holes with high activity, which means that they can react with target gas effectively and efficiently. The new reaction route during the adsorption and desorption process also promotes the enhancement in gas-sensing performance. Therefore, this work prepares an effective gas sensor based on 0.5 at.% Al-ZnOHF for NO<sub>2</sub> detection and provides new insights into modifying ZnOHF-based sensing material with superior gas-sensing performance.

**Supplementary Materials:** The following supporting information can be downloaded at: <https://www.mdpi.com/article/10.3390/ma16093577/s1>, Figure S1: The resistance of samples at different temperatures (a) without and (b) with UV radiation; Figure S2: The dynamic response curve of (a) pure ZnOHF with UV assistance, 100 °C, (b) pure ZnOHF in dark, 160 °C and (c) 0.5 at.% Al-ZnOHF in dark, 160 °C.

**Author Contributions:** X.Y.: Methodology, Investigation, Writing—original draft. R.W.: Data curation, Formal analysis. L.W.: Conceptualization, Project administration, Resources. H.S.: Formal analysis. J.Z.: Funding acquisition and formal analysis. F.L.: Data curation. K.F.: Writing—review and editing. Z.W.: Writing—review and editing. F.W.: Writing—review and editing. J.L.: Visualization and editing. All authors have read and agreed to the published version of the manuscript.

**Funding:** This work was supported by the Natural Foundation of Shandong Province (ZR2022MF311); the National Natural Science Foundation of China (No. 51702188); the Natural Science and Development Foundation of Shenzhen (JCYJ20190807093205660); and the Project Innovation Team of Jinan (2021GXRC036).

**Institutional Review Board Statement:** Not applicable.

**Informed Consent Statement:** Not applicable.

**Data Availability Statement:** The data presented in this study are available on request from the corresponding author. The data are not publicly available due to privacy restrictions.

**Conflicts of Interest:** The authors declare no conflict of interest.

## References

1. Hu, Y.; Li, T.; Zhang, J.; Guo, J.; Wang, W.; Zhang, D. High-sensitive NO<sub>2</sub> sensor based on p-NiCo<sub>2</sub>O<sub>4</sub>/n-WO<sub>3</sub> heterojunctions. *Sens. Actuators B Chem.* **2022**, *352*, 130912. [[CrossRef](#)]
2. Choi, M.S.; Kim, M.Y.; Mirzaei, A.; Kim, H.; Kim, S.; Baek, S.; Chun, D.W.; Jin, C.; Lee, K.H. Selective, sensitive, and stable NO<sub>2</sub> gas sensor based on porous ZnO nanosheets. *Appl. Surf. Sci.* **2021**, *568*, 150910. [[CrossRef](#)]
3. Yang, Z.; Zhang, D.; Chen, H. MOF-derived indium oxide hollow microtubes/MoS<sub>2</sub> nanoparticles for NO<sub>2</sub> gas sensing. *Sens. Actuators B Chem.* **2019**, *300*, 127037. [[CrossRef](#)]
4. Li, W.; Zhang, Y.; Long, X.; Cao, J.; Xin, X.; Guan, X.; Peng, J.; Zheng, X. Gas sensors based on mechanically exfoliated MoS<sub>2</sub> nanosheets for room-temperature NO<sub>2</sub> detection. *Sensors* **2019**, *19*, 2123. [[CrossRef](#)] [[PubMed](#)]
5. Du, W.; Wu, N.; Wang, Z.; Liu, J.; Xu, D.; Liu, W. High response and selectivity of platinum modified tin oxide porous spheres for nitrogen dioxide gas sensing at low temperature. *Sens. Actuators B Chem.* **2018**, *257*, 427–435. [[CrossRef](#)]
6. Nam, B.; Ko, T.; Hyun, S.; Lee, C. NO<sub>2</sub> sensing properties of WO<sub>3</sub>-decorated In<sub>2</sub>O<sub>3</sub> nanorods and In<sub>2</sub>O<sub>3</sub>-decorated WO<sub>3</sub> nanorods. *Nano Converg.* **2019**, *6*, 40. [[CrossRef](#)]
7. Mokrushin, A.; Averin, A.; Gorobtsov, P.; Simonenko, N.; Simonenko, E.; Kuznetsov, N. Obtaining of ZnO/Fe<sub>2</sub>O<sub>3</sub> thin nanostructured films by AACVD for detection of ppb-concentrations of NO<sub>2</sub> as a biomarker of lung infections. *Biosensors* **2023**, *13*, 445. [[CrossRef](#)]
8. Wang, M.; Jin, Z.; Liu, M.; Jiang, G.; Lu, H.; Zhang, Q.; Ju, J.; Tang, Y. Nanoplate-assembled hierarchical cake-like ZnO microstructures: Solvothermal synthesis, characterization and photocatalytic properties. *RSC Adv.* **2017**, *7*, 32528–32535. [[CrossRef](#)]
9. Wang, M.; Sun, T.; Tang, Y.; Jiang, G.; Shi, Y. Template-free synthesis and photocatalytic properties of flower-like ZnOHF nanostructures. *Mater. Lett.* **2015**, *160*, 150–153. [[CrossRef](#)]
10. Mirzaei, A.; Haghghat, F.; Chen, Z.; Yerushalmi, L. Sonocatalytic removal of ampicillin by Zn(OH)F: Effect of operating parameters, toxicological evaluation and by-products identification. *J. Hazard. Mater.* **2019**, *375*, 86–95. [[CrossRef](#)]
11. Chen, H.; Zhu, L.; Hou, Q.; Liang, W.; Liu, H.; Li, W. ZnOHF nanostructure-based quantum dots-sensitized solar cells. *J. Mater. Chem.* **2012**, *22*, 23344. [[CrossRef](#)]
12. Tian, H.; Wang, Y.; Zhang, J.; Ma, Y.; Cui, H.; Cui, Q.; Ma, Y. Compression behavior of copper hydroxyfluoride CuOHF as a case study of the high-pressure responses of the hydrogen-bonded two-dimensional layered materials. *J. Phys. Chem. C* **2019**, *123*, 25492–25500. [[CrossRef](#)]
13. Zhang, G.; Wang, B.; Li, L.; Yang, S. Phosphorus and yttrium co-doped Co(OH)F nanoarray as highly efficient and bifunctional electrocatalysts for overall water splitting. *Small* **2019**, *15*, 1904105. [[CrossRef](#)] [[PubMed](#)]
14. Yao, X.; Zhao, J.; Jin, Z.; Jiang, Z.; Xu, D.; Wang, F.; Zhang, X.; Song, H.; Pan, D.; Chen, Y.; et al. Flower-like hydroxyfluoride-sensing platform toward NO<sub>2</sub> detection. *ACS Appl. Mater. Interfaces* **2021**, *13*, 26278–26287. [[CrossRef](#)] [[PubMed](#)]
15. Mohan, V.; Marappan, G.; Chidambaram, D.; Rajendran, K.; Surya, V.J.; Venugopal, G.; Sivalingam, Y. Photo-enhanced acetone adsorption on delta-MnO<sub>2</sub> nanoparticles: A step towards non-invasive detection of diabetes mellitus. *Mater. Lett.* **2022**, *306*, 130944. [[CrossRef](#)]
16. Chang, J.; Deng, Z.; Li, M.; Wang, S.; Mi, L.; Sun, Q.; Horprathum, M.; He, Y.; Kong, F.; Fang, X.; et al. Visible light boosting hydrophobic ZnO/(Sr<sub>0.6</sub>Bi<sub>0.305</sub>)<sub>2</sub>Bi<sub>2</sub>O<sub>7</sub> chemiresistor toward ambient trimethylamine. *Sens. Actuators B Chem.* **2022**, *352*, 131076. [[CrossRef](#)]
17. Wang, M.; Zhu, Y.; Luo, Q.; Ge, C.; Liu, G.; Qiao, G.; Kim, E.J. Below-room-temperature solution-grown ZnO porous nanosheet arrays with ppb-level NO<sub>2</sub> sensitivity under intermittent UV irradiation. *Appl. Surf. Sci.* **2021**, *566*, 150750. [[CrossRef](#)]
18. Zhang, D.; Yu, S.; Wang, X.; Huang, J.; Pan, W.; Zhang, J.; Meteku, B.E.; Zeng, J. UV illumination-enhanced ultrasensitive ammonia gas sensor based on (001) TiO<sub>2</sub>/MXene heterostructure for food spoilage detection. *J. Hazard. Mater.* **2022**, *423*, 127160. [[CrossRef](#)]
19. Anbalagan, A.K.; Gupta, S.; Kumar, R.R.; Tripathy, A.R.; Chaudhary, M.; Haw, S.; Murugesan, T.; Lin, H.; Chueh, Y.; Tai, N.; et al. Gamma-ray engineered surface defects on zinc oxide nanorods towards enhanced NO<sub>2</sub> gas sensing performance at room temperature. *Sens. Actuators B Chem.* **2022**, *369*, 132255. [[CrossRef](#)]
20. Bang, J.H.; Kwon, Y.J.; Lee, J.; Mirzaei, A.; Lee, H.Y.; Choi, H.; Kim, S.S.; Jeong, Y.K.; Kim, H.W. Proton-beam engineered surface-point defects for highly sensitive and reliable NO<sub>2</sub> sensing under humid environments. *J. Hazard. Mater.* **2021**, *416*, 125841. [[CrossRef](#)]
21. Wang, G.; He, Z.; Shi, G.; Wang, H.; Zhang, Q.; Li, Y. Controllable construction of Titanium dioxide-Zirconium dioxide@Zinc hydroxyfluoride networks in micro-capillaries for bio-analysis. *J. Colloid Interface Sci.* **2015**, *446*, 290–297. [[CrossRef](#)] [[PubMed](#)]

22. Peng, Y.; Zhou, H.; Wang, Z. Synthesis, characterization and photocatalytic activity of Zn(OH)F hierarchical nanofibers prepared by a simple solution-based method. *CrystEngComm* **2012**, *14*, 2812–2816. [[CrossRef](#)]
23. Eadi, S.B.; Shin, H.; Kumar, P.S.; Song, K.; Yuvakkumar, R.; Lee, H. Fluorine-implanted indium-gallium-zinc oxide (IGZO) chemiresistor sensor for high-response NO<sub>2</sub> detection. *Chemosphere* **2021**, *284*, 131287. [[CrossRef](#)] [[PubMed](#)]
24. Li, X.; Wang, Y.; Cheng, P.; Liu, Y.; Lei, Z.; Liu, M.; Yao, X.; Yan, H.; Weng, Z. Multicore-shell structured Ce-In<sub>2</sub>O<sub>3</sub> for acetone detection by spray pyrolysis using NaCl as a high temperature auxiliary agent. *Mater. Chem. Front.* **2021**, *6*, 213–224. [[CrossRef](#)]
25. Mokoena, T.P.; Swart, H.C.; Hillie, K.T.; Motaung, D.E. Engineering of rare-earth Eu<sup>3+</sup> ions doping on p-type NiO for selective detection of toluene gas sensing and luminescence properties. *Sens. Actuators B Chem.* **2021**, *347*, 130530. [[CrossRef](#)]
26. Qin, C.; Wang, B.; Wang, Y. Metal-organic frameworks-derived Mn-doped Co<sub>3</sub>O<sub>4</sub> porous nanosheets and enhanced CO sensing performance. *Sens. Actuators B Chem.* **2022**, *351*, 130943. [[CrossRef](#)]
27. Mokrushin, A.S.; Nagornov, I.A.; Simonenko, T.L.; Simonenko, N.P.; Gorobtsov, P.Y.; Arkhipushkin, I.A.; Simonenko, E.P.; Sevastyanov, V.G.; Kuznetsov, N.T. Gas-sensitive nanostructured ZnO films praseodymium and europium doped: Electrical conductivity, selectivity, influence of UV irradiation and humidity. *Appl. Surf. Sci.* **2022**, *589*, 152974. [[CrossRef](#)]
28. Sun, J.; Wang, Y.; Song, P.; Yang, Z.; Wang, Q. Metal-organic framework-derived Cr-doped hollow In<sub>2</sub>O<sub>3</sub> nanoboxes with excellent gas-sensing performance toward ammonia. *J. Alloys Compd.* **2021**, *879*, 160472. [[CrossRef](#)]
29. Nagarjuna, Y.; Lin, J.; Wang, S.; Hsiao, W.; Hsiao, Y. AZO-based ZnO nanosheet MEMS sensor with different Al concentrations for enhanced H<sub>2</sub>S gas sensing. *Nanomaterials* **2021**, *11*, 3377. [[CrossRef](#)]
30. Ramgir, N.S.; Goyal, C.P.; Goyal, D.; Patil, S.J.; Ikeda, H.; Ponnusamy, S.; Muthe, K.P.; Debnath, A.K. NO<sub>2</sub> sensor based on Al modified ZnO nanowires. *Mater. Sci. Semicond. Process.* **2021**, *134*, 106027. [[CrossRef](#)]
31. Jaballah, S.; Alaskar, Y.; AlShunaifi, I.; Ghiloufi, I.; Neri, G.; Bouzidi, C.; Dahman, H.; El Mir, L. Effect of Al and Mg doping on reducing gases detection of ZnO nanoparticles. *Chemosensors* **2021**, *9*, 300. [[CrossRef](#)]
32. Bulut, F.; Ozturk, O.; Acar, S.; Yildirim, G. Effect of Ni and Al doping on structural, optical, and CO<sub>2</sub> gas sensing properties of 1D ZnO nanorods produced by hydrothermal method. *Microsc. Res. Tech.* **2021**, *85*, 1502–1517. [[CrossRef](#)] [[PubMed](#)]
33. Liu, F.; Huang, G.; Wang, X.; Xie, X.; Xu, G.; Lu, G.; He, X.; Tian, J.; Cui, H. High response and selectivity of single crystalline ZnO nanorods modified by In<sub>2</sub>O<sub>3</sub> nanoparticles for n-butanol gas sensing. *Sens. Actuators B Chem.* **2018**, *277*, 144–151. [[CrossRef](#)]
34. Mu, Y.; Zhou, T.; Li, D.; Liu, W.; Jiang, P.; Chen, L.; Zhou, H.; Ge, G. Highly stable and durable Zn-metal anode coated by bi-functional protective layer suppressing uncontrollable dendrites growth and corrosion. *Chem. Eng. J.* **2022**, *430*, 132839. [[CrossRef](#)]
35. Tian, X.; Yao, L.; Cui, X.; Zhao, R.; Xiao, X.; Wang, Y. Novel Al-doped CdIn<sub>2</sub>O<sub>4</sub> nanofibers based gas sensor for enhanced low-concentration n-butanol sensing. *Sens. Actuators B Chem.* **2022**, *351*, 130946. [[CrossRef](#)]
36. Zhu, B.; Liu, Y.; Zhao, H.; Zhang, X.; He, P.; Wu, L.; Liu, Y.; Yang, T. ZnOHf/N-doped carbon hybrids as a novel anode material for enhanced lithium storage. *J. Alloys Compd.* **2021**, *889*, 161705. [[CrossRef](#)]
37. Du, W.; Si, W.; Du, W.; Ouyang, T.; Wang, F.; Gao, M.; Wu, L.; Liu, J.; Qian, Z.; Liu, W. Unraveling the promoted nitrogen dioxide detection performance of N-doped SnO<sub>2</sub> microspheres at low temperature. *J. Alloys Compd.* **2020**, *834*, 155209. [[CrossRef](#)]
38. Wang, Y.; Liu, B.; Xiao, S.; Wang, X.; Sun, L.; Li, H.; Xie, W.; Li, Q.; Zhang, Q.; Wang, T. Low-temperature H<sub>2</sub>S detection with hierarchical Cr-doped WO<sub>3</sub> microspheres. *ACS Appl. Mater. Inter.* **2016**, *8*, 9674–9683. [[CrossRef](#)]
39. Zhang, Z.; Haq, M.; Wen, Z.; Ye, Z.; Zhu, L. Ultrasensitive ppb-level NO<sub>2</sub> gas sensor based on WO<sub>3</sub> hollow nanospheres doped with Fe. *Appl. Surf. Sci.* **2018**, *434*, 891–897. [[CrossRef](#)]
40. Jiang, T.; Liu, X.; Sun, J. UV-enhanced NO<sub>2</sub> sensor using ZnO quantum dots sensitized SnO<sub>2</sub> porous nanowires. *Nanotechnology* **2022**, *33*, 185501. [[CrossRef](#)]
41. Zhang, Q.; Pang, Z.; Hu, W.; Li, J.; Liu, Y.; Liu, Y.; Yu, F.; Zhang, C.; Xu, M. Performance degradation mechanism of the light-activated room temperature NO<sub>2</sub> gas sensor based on Ag-ZnO nanoparticles. *Appl. Surf. Sci.* **2021**, *541*, 148418. [[CrossRef](#)]
42. Paolucci, V.; De Santis, J.; Lozzi, L.; Rigon, M.; Martucci, A.; Cantalini, C. ZnO thin films containing aliovalent ions for NO<sub>2</sub> gas sensor activated by visible light. *Ceram. Int.* **2021**, *47*, 25017–25028. [[CrossRef](#)]
43. Sun, K.; Zhan, G.; Chen, H.; Lin, S. Low-operating-temperature NO<sub>2</sub> sensor based on a CeO<sub>2</sub>/ZnO heterojunction. *Sensors* **2021**, *21*, 8269. [[CrossRef](#)] [[PubMed](#)]
44. Liang, Y.; Hsu, Y. Enhanced sensing ability of brush-like Fe<sub>2</sub>O<sub>3</sub>-ZnO nanostructures towards NO<sub>2</sub> gas via manipulating material synergistic effect. *Int. J. Mol. Sci.* **2021**, *22*, 6884. [[CrossRef](#)]
45. Chen, L.; Song, Y.; Liu, W.; Dong, H.; Wang, D.; Liu, J.; Liu, Q.; Chen, X. MOF-based nanoscale Pt catalyst decorated SnO<sub>2</sub> porous nanofibers for acetone gas detection. *J. Alloys Compd.* **2022**, *893*, 162322. [[CrossRef](#)]
46. Liang, J.; Wu, W.; Lou, Q.; Wang, K.; Xuan, C. Room temperature NO<sub>2</sub> sensing performance of Ag nanoparticles modified VO<sub>2</sub> nanorods. *J. Alloys Compd.* **2022**, *890*, 161837. [[CrossRef](#)]
47. Navarrete, E.; Guell, F.; Martinez-Alanis, P.R.; Llobet, E. Chemical vapour deposited ZnO nanowires for detecting ethanol and NO<sub>2</sub>. *J. Alloys Compd.* **2022**, *890*, 161923. [[CrossRef](#)]
48. Xu, F.; HO, H. Light-activated metal oxide gas sensors: A review. *Micromachines* **2017**, *8*, 333. [[CrossRef](#)]
49. Benamara, M.; Massoudi, J.; Dahman, H.; Ly, A.; Dhahri, E.; Debliqy, M.; El Mir, L.; Lahem, D. Study of room temperature NO<sub>2</sub> sensing performances of ZnO<sub>1-x</sub> (x = 0, 0.05, 0.10). *Appl. Phys. A* **2022**, *128*, 31. [[CrossRef](#)]
50. Šetka, M.; Claros, M.; Chmela, O.; Vallejos, S. Photoactivated materials and sensors for NO<sub>2</sub> monitoring. *J. Mater. Chem. C* **2021**, *9*, 16804–16827. [[CrossRef](#)]

51. Chen, X.; Hu, J.; Chen, P.; Yin, M.; Meng, F.; Zhang, Y. UV-light-assisted NO<sub>2</sub> gas sensor based on WS<sub>2</sub>/PbS heterostructures with full recoverability and reliable anti-humidity ability. *Sens. Actuators B Chem.* **2021**, *339*, 129902. [[CrossRef](#)]
52. Hung, N.M.; Hung, C.M.; Van Duy, N.; Hoa, N.D.; Hong, H.S.; Dang, T.K.; Viet, N.N.; Thing, L.V.; Phuoc, P.H.; Van Hieu, N. Significantly enhanced NO<sub>2</sub> gas-sensing performance of nanojunction-networked SnO<sub>2</sub> nanowires by pulsed UV-radiation. *Sens. Actuators A Phys.* **2021**, *327*, 112759. [[CrossRef](#)]
53. Kamble, V.S.; Navale, Y.H.; Patil, V.B.; Desai, N.K.; Vajekar, S.N.; Salunkhe, S.T. Studies on structural, spectral and morphological properties of co-precipitation derived Co-doped ZnO nanocapsules for NO<sub>2</sub> sensing applications. *J. Mater. Sci. Mater. Electron.* **2021**, *32*, 26503–26519. [[CrossRef](#)]

**Disclaimer/Publisher's Note:** The statements, opinions and data contained in all publications are solely those of the individual author(s) and contributor(s) and not of MDPI and/or the editor(s). MDPI and/or the editor(s) disclaim responsibility for any injury to people or property resulting from any ideas, methods, instructions or products referred to in the content.